LAWRENCE
LIVERMORE
NATIONAL
LABORATORY

LLNL-PROC-420389

# HRTEM Study of Oxide Nanoparticles in 16Cr-4Al-2W-0.3Ti-0.3Y2O3 ODS Steel

L. Hsiung, M. Fluss, M. Wall, A. Kimura

November 18, 2009

2009 MRS Fall Meeting
Boston, MA, United States
November 29, 2009 through December 4, 2009

## Disclaimer

# HRTEM Study of Oxide Nanoparticles in 16Cr-4Al-2W-0.3Ti-0.3$Y_2O_3$ ODS Steel

Luke L. Hsiung[1], Michael J. Fluss[1], Mark A. Wall[1], Akihiko Kimura[2]

[1]Lawrence Livermore National Laboratory
Physical and Life Sciences Directorate
L-352, P.O. Box 808
Livermore, CA, U.S.A.

[2]Institute of Advanced Energy
Kyoto University, Gokasho, Uji
Kyoto 611-0011, Japan

## ABSTRACT

Crystal and interfacial structures of oxide nanoparticles in 16Cr-4Al-2W-0.3Ti-0.3$Y_2O_3$ ODS ferritic steel have been examined using high-resolution transmission electron microscopy (HRTEM) techniques. Oxide nanoparticles with a complex-oxide core and an amorphous shell were frequently observed. The crystal structure of complex-oxide core is identified to be mainly monoclinic $Y_4Al_2O_9$ (YAM) oxide compound. Orientation relationships between the oxide and matrix are found to be dependent on the particle size. Large particles (> 20 nm) tend to be incoherent and have a spherical shape, whereas small particles (< 10 nm) tend to be coherent or semi-coherent and have a faceted interface. The observations of partially amorphous nanoparticles lead us to propose three-stage mechanisms to rationalize the formation of oxide nanoparticles containing core/shell structures in as-fabricated ODS steels.

## INTRODUCTION

Development of high-performance structural materials for first wall and breeding-blanket components, which will be exposed to high fluxes of high energy (14 MeV) neutrons from the deuterium-tritium fusion, is one of the major challenges in materializing future fusion reactors. The choice of structural materials for the first wall and blanket to a large degree dictates the design of the reactor systems. The selection of suitable structural materials is based on conventional properties (such as thermophysical, mechanical, and corrosion and compatibility), low neutron-induced radioactivity, and resistance to radiation-induced damage phenomena like material hardening/embrittlement and/or dimensional instability caused by void- and helium-driven swelling [1]. Oxide dispersion strengthened (ODS) ferritic/martensitic and ferritic steels produced by mechanical alloying of the elemental or pre-alloyed powders of metallic matrix complemented with an adequate quantity of yttria ($Y_2O_3$) powder consolidated by hot extrusion or hot isostatic pressing are advanced structural materials with a potential to be used at elevated temperatures due to the dispersion of thermally stable oxide nanoparticles into the ferritic/martensitic matrix. The use of ODS steels should improve creep strength and oxidation/corrosion resistance at high temperatures and consequently increase the operating temperature of first wall and blanket structures in the future fusion/fission hybrid reactors by approximately 700 ºC or higher [2]. The performance of ODS steels is largely determined by the particle size and the stability of dispersed oxide nanoparticles. Although $Y_2O_3$ has been selected as the major dispersed oxide, its particle size increases during the consolidation and thermomechanical treatment of ODS steels. To enhance the stability of oxide particles, titanium and aluminum are added to form complex oxide with $Y_2O_3$ so as to make the dispersed oxides finer and more stable [2, 3]. Complex mechanisms involving fragmentation, dissolution of $Y_2O_3$ particles, and precipitation of complex-oxide nanoparticles were previously proposed by Okuda and Fujiwara [4], Kimura et al. [5] and Sakasegawa et al. [6] based on the results generated from x-ray diffraction and conventional TEM studies. However, recent studies conducted by Marquis [7] using 3-D atom probe tomography and Klimiankou et al. [8] using EDX and EELS methods have revealed the existence of a complex-oxide core structure associated with a solute-enriched shell structure in oxide nanoparticles. The existence of core/shell structures in nanoparticles however challenges the accountability of previously proposed dissolution/precipitation mechanisms. HRTEM study of nanoparticles in K3-ODS was thus conducted to examine the crystal and interfacial structures of oxide nanoparticles to better understand the formation mechanisms of oxide nanoparticles associated with core/shell structures.

## EXPERIMENTAL

The materials used for this investigation was 16Cr-4Al-2W-0.3Ti-0.3$Y_2O_3$ (K3) ODS ferritic steel [9]. Details of the fabrication process of the ODS steels can be found elsewhere [10]. Briefly, the pre-alloyed powder was first mechanically alloyed with $Y_2O_3$ powder in an Argon gas atmosphere at room temperature using an attrition type ball mill. The powder was

then sealed in a stainless-steel can and degassed at 400 °C in 0.1 Pa vacuum. The canned powders were subsequently consolidated by a hot extrusion technique at 1150 °C. After the extrusion, the consolidated ODS steel was thermally treated at 1050 °C for 1 hour. One K3-ODS steel sample was also annealed at 900 °C, 168 hours (one week) for a thermal stability study. The chemical composition (in wt.%) of the consolidated material is C: 0.08, Si: 0.033, Cr: 16, W: 1.82, Al: 4.59, Ti: 0.28, $Y_2O_3$: 0.368, and Fe: balance [9]. Thin foils for TEM analysis were prepared by a standard procedure that includes slicing, grinding, and polishing the recovered fragments with the foils surface approximately perpendicular to the loading axis. Final thinning of the foils was performed using a standard twin-jet electropolishing technique in an electrolyte (90 vol.% acetic acid, 10 vol.% perchloric acid) at 30 V and room temperature. Microstructural characterization was performed using Phillips CM300 field-emission transmission electron microscope (accelerating voltage of 300 kV). A software package CaRIne Crystallography 3.1 was used to simulate electron diffraction patterns in order to identify the crystal structures of ODS nanoparticles.

## RESULTS AND DISCUSSION

Typical microstructures of K3-ODS steel are shown in Figs. 1a and 1b. Here, elongated grains (Fig. 1a) and dense oxide nanoparticles (Fig. 1b), mainly $Y_4Al_2O_9$ (YAM) complex oxide, were observed. The oxide nanoparticle sizes in K3-ODS (Fig. 1b) are typically ranging from 1.7 nm to 30 nm, with a mean particle size of 5.91 nm, and a particle density of 1.33 x $10^{22}$ $m^{-3}$. It is worth noting that few particles with sizes larger than 30 nm were also observed; those particles were identified to be mostly the remnants of original $Y_2O_3$ particles. Here the orientation relationship between $Y_4Al_2O_9$ oxide phase and the matrix can be derived from the selected-area diffraction pattern: $(0\bar{1}1)_\alpha \parallel (2\bar{4}2)_{YAM}$ and $[011]_\alpha \parallel [432]_{YAM}$. The formation of $Y_4Al_2O_9$ oxide particles was identified and confirmed by matching several observed and simulated diffraction patterns of different zone axes, and an example is shown in Fig. 2 for the $[432]_{YAM}$-zone pattern. $Y_4Al_2O_9$ has a monoclinic structure and space group: $P2_1/c$ with a = 0.7375 nm, b = 1.0507 nm, c = 1.1113 nm, and β = 108.58° [11, 12], which is illustrated in Fig. 2c. By comparing the $Y_4Al_2O_9$ nanoparticles formed in the ODS steel with the starting $Y_2O_3$ particles (space group: $Ia_3$, a cubic structure with $a_o$ = 1.06 nm [12], particle size: 15-30 nm [13]) used to fabricate the ODS steel, one can realize that the formation of oxide nanoparticles in ODS steels does not take place solely through a fragmentation mechanism. The formation of $Y_4Al_2O_9$ oxide reveals the occurrence of an internal oxidation reaction: $2Y_2O_3 + Al_2O_3 \rightarrow Y_4Al_2O_9$ during consolidation, which is governed by the oxygen affinity of alloying elements. That is, the formation of Y-Al complex oxides becomes predominant when both Al and Ti are present in ODS steels, which is in agreement with a conclusion made by Kasada et al [3].

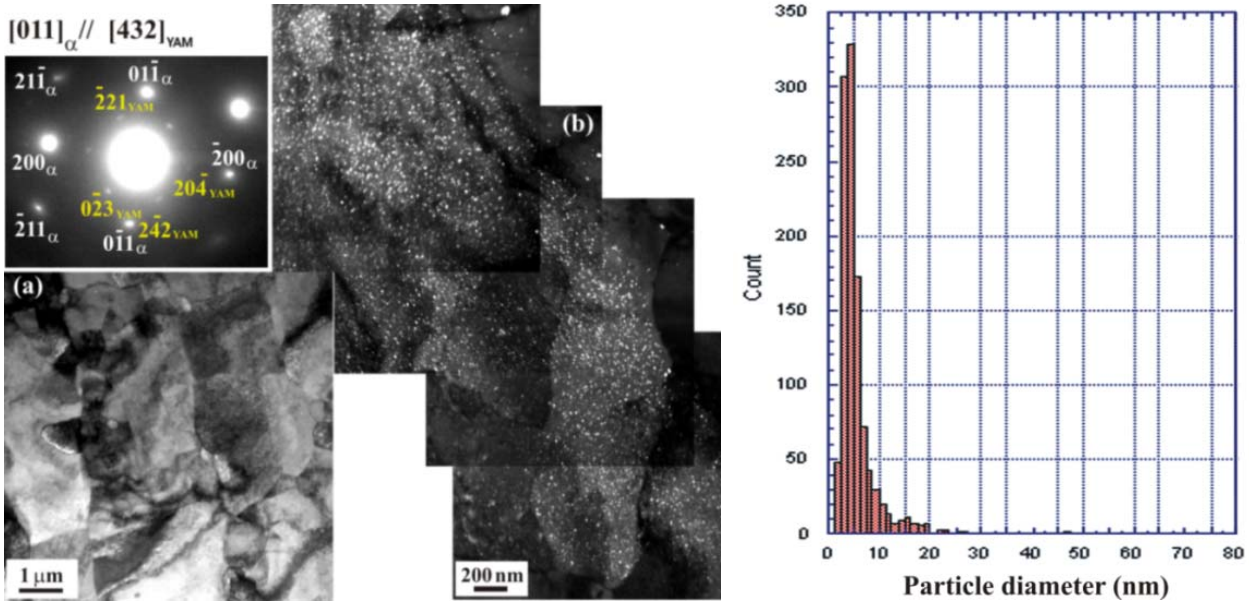


Fig. 1. (a) Bright-field TEM image shows typical grain morphology of K3-ODS steel, (b) dark-field TEM image and selected-area diffraction pattern of the $[011]_{Fe\text{-}Cr(\alpha)} \parallel [432]_{YAM}$-zone show the formation of dense $Y_4Al_2O_9$ nanoparticles in K3-ODS steel. (b) Size distribution of oxide nanoparticles evaluated from TEM micrographs.

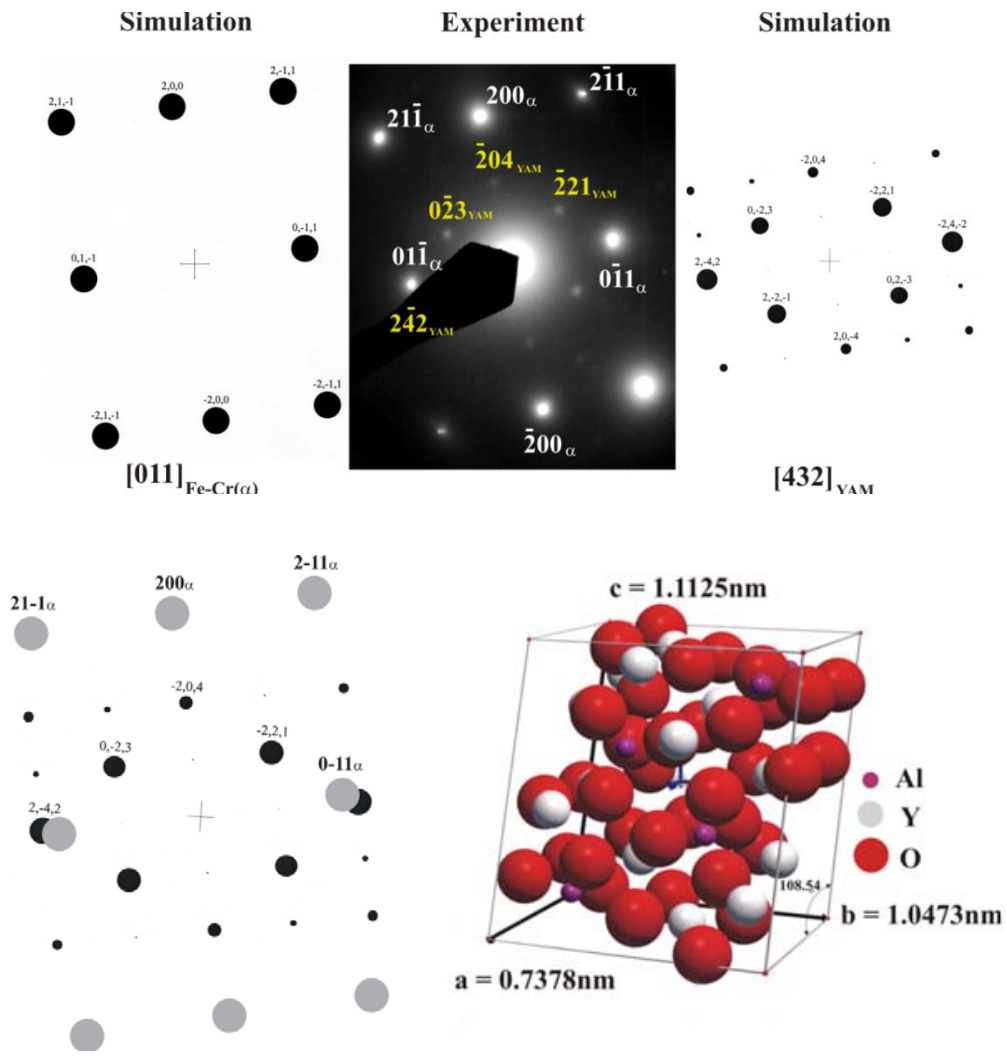


Fig. 2. (a) Observed and simulated diffraction patterns of the $[011]_{Fe\text{-}Cr(\alpha)}$-zone and the $[432]_{YAM}$-zone for identifying the formation of $Y_4Al_2O_9$ complex-oxide nanoparticles; (b) overlap of the simulated $[011]_{Fe\text{-}Cr(\alpha)}$-zone and $[432]_{YAM}$-zone patterns; (c) crystal structure of $Y_4Al_2O_9$ oxide compound .

HRTEM images of a large (> 20 nm) and a small (< 10 nm) nanoparticles in K3-ODS steel sample are shown in Figs. 3a and 3b. As can be seen in Fig. 3a, the large nanoparticle tends to be near spherical in shape and is incoherent with the matrix. In addition, one can also distinguish the core region with an appearance of lattice fringes from the outer shell region with a featureless appearance (presumably due to amorphization that will be discussed below), although the shell region does not appear to have a uniform thickness. On the other hand, ledges and facets can be seen at the interface between the small nanoparticle and the matrix shown in Fig. 3b, which indicates that the small nanoparticle tends to be coherent or semi-coherent with the matrix. A very thin layer of featureless domain can also be found on the left-hand side of the oxide/matrix interface, which will be shown later. Figure 4 sheds some light on why featureless domains at the oxide/matrix interfaces form. Here nucleation of a crystalline $Y_4Al_2O_9$ domain (2 x 5 nm in size) can be clearly seen within an amorphous oxide particle. In addition, several arrays of atoms can be found to align parallel to the $(0\bar{2}3)_{YAM}$ plane on the left hand side of the amorphous oxide particle. Orientation relationship between the crystalline $Y_4Al_2O_9$ domain and the matrix, which is the same as that shown in Figs. 1 and 2, can be derived from the fast Fourier transformation (FFT) image: $(0\bar{1}1)_\alpha \parallel (2\bar{4}2)_{YAM}$ and $[011]_\alpha \parallel [432]_{YAM}$. Figures 6a and 6b present interfacial structures of the small nanoparticles in Fig. 3b and Fig. 4, respectively. Facets, ledges, interface dislocations, and thin layer of amorphous domains (marked by red arrows) are common features that can be found among the two interfaces. Orientation relationship between the $Y_4Al_2O_9$ oxide and the matrix in Fig. 5a, which is different from that shown in Fig. 4, can be derived from the FFT image: $(0\bar{1}1)_\alpha \parallel (\bar{1}\bar{1}5)_{YAM}$ and $[011]_\alpha \parallel [732]_{YAM}$. These two different orientation relationships between the $Y_4Al_2O_9$ nanoparticle and the matrix reveal that the {011} planes of the matrix act as a habit plane for the nucleation of $Y_4Al_2O_9$ nanoparticles.

Figure 6 shows the result of an ODS steel sample annealed at 900 °C for 168 hours. Here a small nanoparticle (< 10 nm) remains faceted and a large nanoparticle (> 20 nm) becomes perfectly spherical without a core/shell structure. The observation of oxide nanoparticle without a core/shell structure after prolonged annealing seems to suggest that the core/shell structures of oxide nanoparticles formed in the as-fabricated ODS steels are far from chemical equilibrium. Formation mechanisms of ODS nanoparticles are accordingly proposed based on the above HRTEM observations. The formation mechanisms basically include the following three stages: (1) Fragmentation of starting $Y_2O_3$ particles to form finely-dispersed (nano or sub-nano) fragments during ball milling; (2) Agglomeration and amorphization of fragments mixed with matrix material to form clusters and agglomerates (designated as [MYO], M: alloying elements) during ball milling; (3) Crystallization of the amorphous oxide agglomerates to form oxide nanoparticles with a complex-oxide core and a solute-enriched (M′) shell. The contents of complex-oxide core and solute-enriched shell are dependent on the compositions of different ODS steels. Y-Al complex-oxide ($Y_xAl_yO_z$) core can form in Al-contained ODS steels, Y-Ti complex-oxide ($Y_xTi_yO_z$) core can form in Ti-contained ODS steels with no addition of Al, and $Y_2O_3$ core can form in ODS steels with no additions of Al and Ti. The solute-enriched shell can be perceived as a result of the depletion of the solutes that are not involved in the oxidation reactions for the complex-oxide core. The shell thickness is dependent on the size of nanoparticles since the larger the particle the more matrix material will participate in the agglomeration and amorphization stage and thus more solutes will be depleted from the oxide core during the crystallization stage. A solute-enriched shell forms when solute depletion rate from the core is greater than solute diffusion rate from the oxide/matrix interface during the crystallization stage.

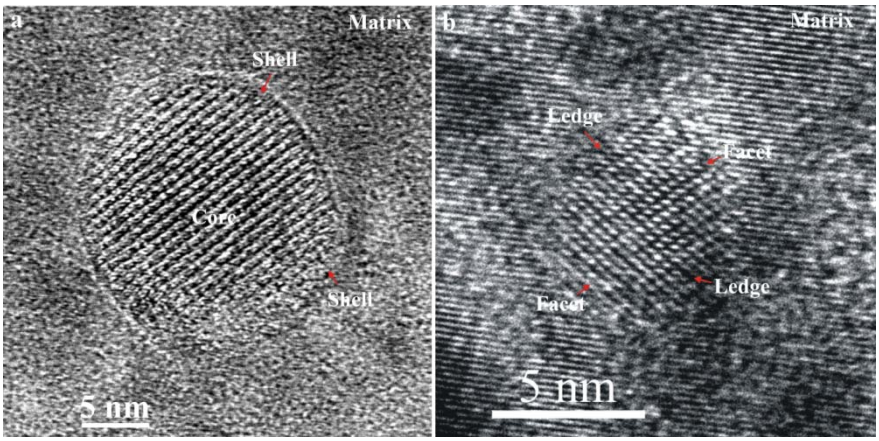


Fig. 3. HRTEM images of (a) a large nanoparticle (> 20 nm): incoherent interface associated with a core/shell structure and (b) small nanoparticles (< 10 nm): semi-coherent interfaces associated with facets and ledges.

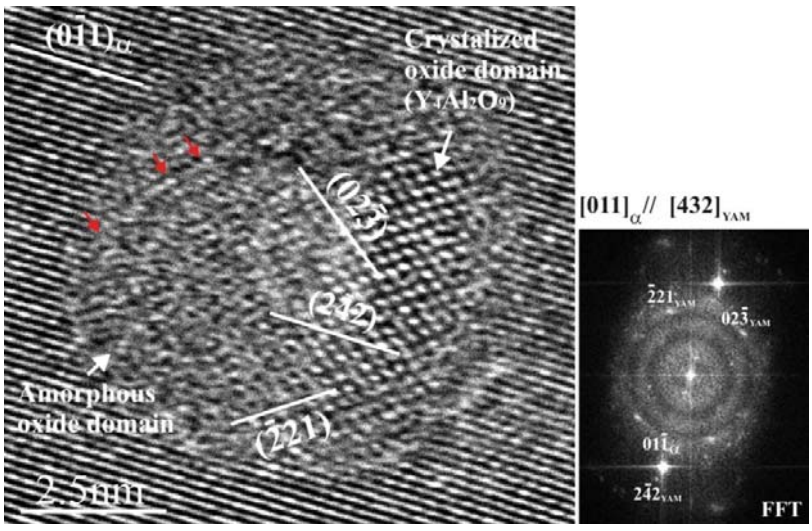


Fig. 4. HRTEM image shows the nucleation of a crystalline $Y_4Al_2O_9$ domain (2 x 5 nm) in an amorphous oxide particle; facets, ledges, and thin shell of amorphous domains (marked by red arrows) can be found at the oxide/matrix interface. Orientation relationship between the $Y_4Al_2O_9$ crystal and matrix can be derived from the FFT image.

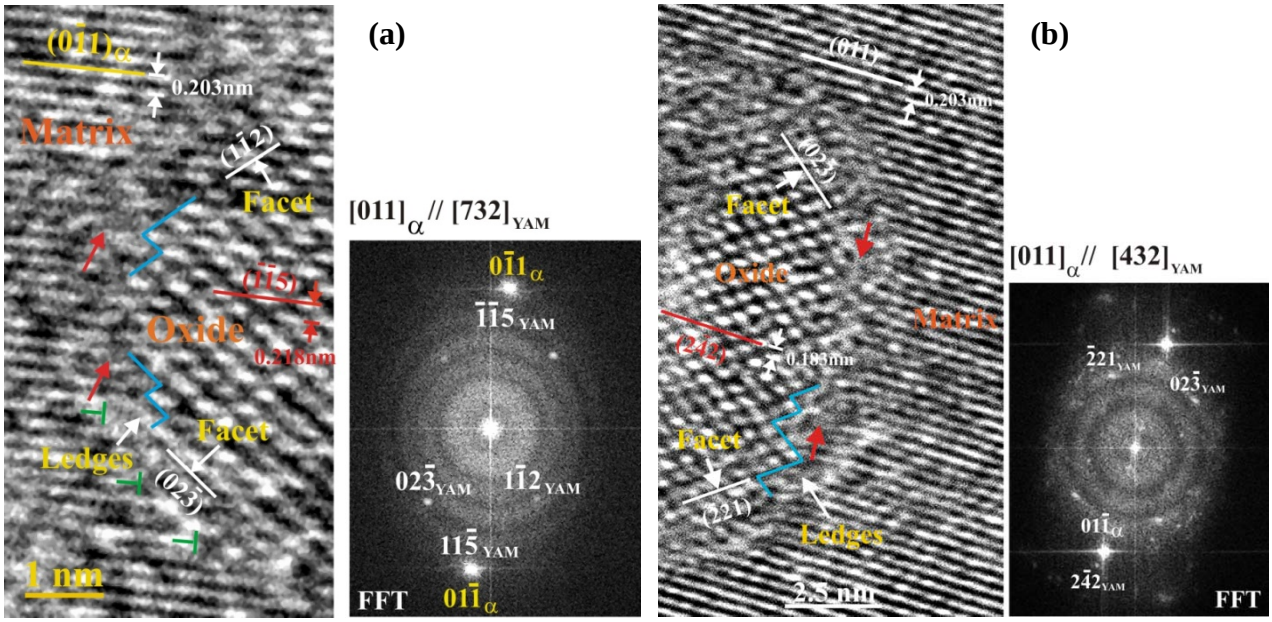


Fig. 5. HRTEM images show (a) structure of interface between the oxide nanoparticle and matrix in Fig. 3b and (b) structure of interface between the crystalline domain and matrix in Fig. 4. Facets, ledges, dislocations, and thin layer of featureless domains (marked by red arrows) can be readily found at the interfaces. Two different orientation relationships between $Y_4Al_2O_9$ oxide and matrix were derived from the FFT images.

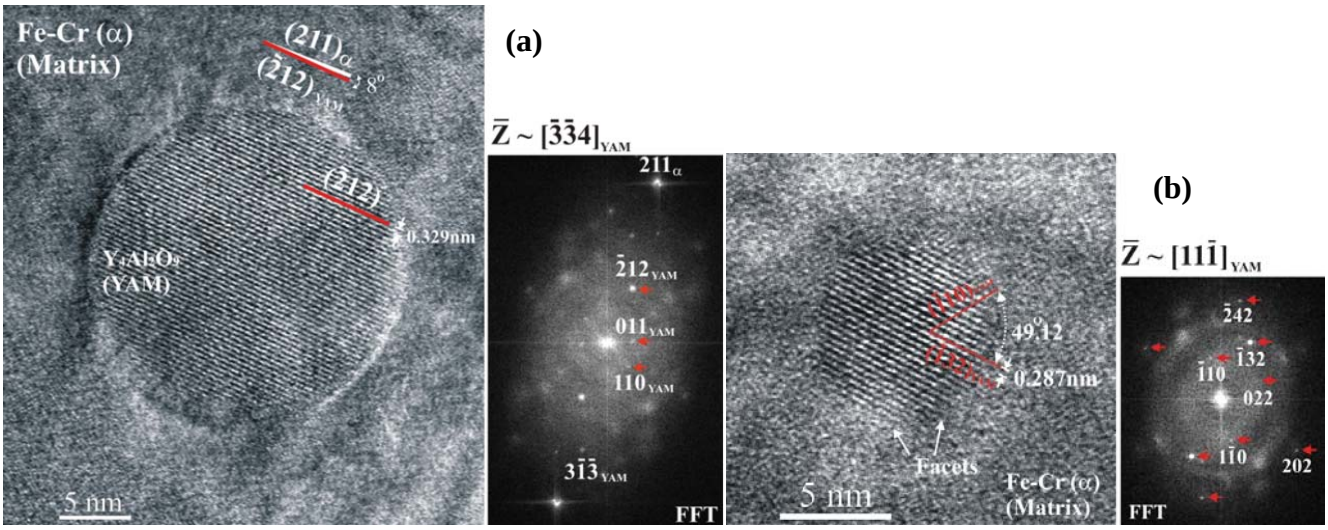


Fig. 6. HRTEM images of (a) a large $Y_4Al_2O_9$ nanoparticle (> 20 nm) and (b) a small nanoparticle (< 10 nm) after prolonged annealing at 900 °C for 168 hours. Notice that the small nanoparticle remains faceted and the large nanoparticle becomes perfectly spherical without a core/shell structure.

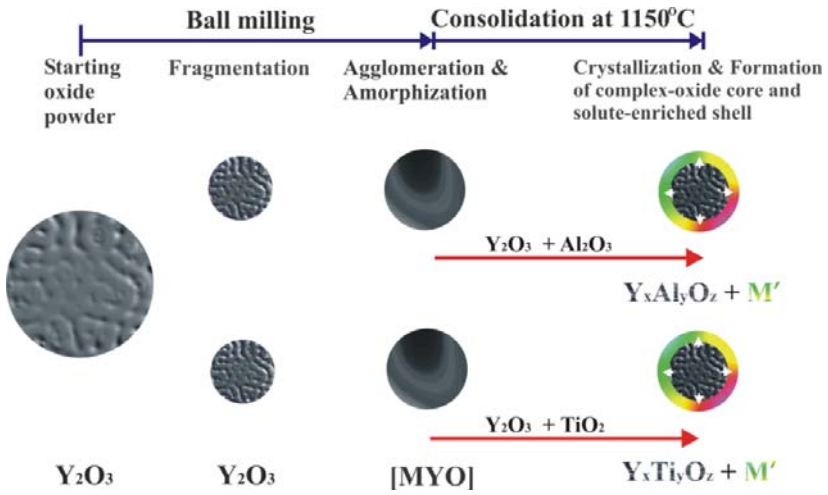


Fig. 7. Schematics of the proposed three-stage mechanisms for the formation of oxide nanoparticles containing a core/shell structure during a mechanical alloying process; a solute-enriched shell forms when solute depletion rate from the core is greater than solute diffusion rate from the oxide/matrix interface during the crystallization stage. Note that the nucleation of a spherical core at the center of a spherical particle is only indicated for an illustration purpose.

## CONCLUSION

The oxide nanoparticles formed in 16Cr-4Al-2W-0.3Ti-0.3$Y_2O_3$ (K3) ODS steel are mainly $Y_4Al_2O_9$ (YAM) with a monoclinic structure. Large nanoparticles (> 20 nm) usually have a spherical shape and tend to be incoherent with the matrix; small nanoparticles (< 10 nm) usually accompany with facets and ledges at the oxide/matrix interfaces and tend to be coherent or semi-coherent with the matrix. A structure of $Y_4Al_2O_9$ oxide core associated with amorphous shell forms in both large and small nanoparticles in the as-fabricated ODS steel. The core/shell structure becomes diminished after prolonged annealing at 900 °C for 168 hours, which suggests that the core/shell structures of oxide nanoparticles are far from chemical equilibrium. Three-stage formation mechanisms of ODS nanoparticles are accordingly proposed to rationalize the formation of core/shell structures.

## ACKNOWLEDGEMENTS

This work was performed under the auspices of the U.S. Department of Energy by Lawrence Livermore National Laboratory under Contract DE-AC52-07NA27344. Work at LLNL was funded by the Laboratory Directed Research and Development Program at LLNL under project tracking code 09-SI-003. The authors gratefully acknowledge Nick E. Teslich and Rick J. Gross for their efforts on TEM sample preparation.

## REFERENCES

1. K. Ehrlich, Phil. Trans. R. Soc. Lond. A 357 (1999) 595.
2. S. Ukai, M. Fujiwara, J. Nucl. Mater. 307-311 (2002) 749.
3. R. Kasada, N. Toda, K. Yutani, H.S. Cho, H. Kishimoto, A. Kimura, J. Nucl. Mater. 341 (2005) 103.
4. T. Okuda, M. Fujiwara, J. Mater. Sci. Lett. 14 (1995) 1600.
5. Y. Kimura, S. Takaki, S. Suejima, R. Uemori, H. Tamehiro, ISIJ International, 39 (2) (1999) 176.
6. H. Sakasegawa, M. Tamura, S. Ohtsuka, S. Ukai, H. Tanigawa, A. Kohyama, M. Fujiwara, J. Alloys & Compounds 452 (2008) 2.
7. E. A. Marquis, Appl. Phys. Lett. 93 (2008) 181904.
8. M. Klimiankou, R. Lindau, A. Möslang, J. Nucl. Mater. 386-388 (2009) 553.
9. K. Yutani, H. Kishimoto, R. Kasada, A. Kimura, J. Nucl. Mater. 367-370 (2007) 423.
10. S. Uki, T. Nishida, H. Okada, T. Okuda, M. Fujiwara, K. Asabe, J. Nucl. Sci. Technol. 34 (3) (1997) 256.
11. A. Nørlund Christensen and R.G. Hazell, Acta Chemica Scandinavica **45** (1991) 226.
12. W.Y. Ching, Y.N. Xu, Physical Review B 59 (20) (1999) 12815.
13. V. de Castro, T. Leguey, M.A. Monge, A. Munoz, R. Pareja, D.R. Amador, J.M. Torralba, M. Victoria, J. Nucl. Mater. 322 (2003) 228.